Mode hybridization in DNA-inspired helical metamaterials with variable centro-asymmetry ⓕ

ⓘD Gunho Kim, ⓘD Kaila M. Y. Coimbra and ⓘD Chiara Daraio

COLLECTIONS

ⓕ This paper was selected as Featured

View Online   Export Citation   CrossMark

ARTICLES YOU MAY BE INTERESTED IN

Tunable auxetic metamaterials for simultaneous attenuation of airborne sound and elastic vibrations in all directions
Applied Physics Letters 121, 081702 (2022); https://doi.org/10.1063/5.0104266

Inertially amplified seismic metamaterial with an ultra-low-frequency bandgap
Applied Physics Letters 121, 081701 (2022); https://doi.org/10.1063/5.0102821

Reversible topological non-reciprocity by positive–negative Poisson's ratio switch in chiral metamaterials
Applied Physics Letters 121, 071702 (2022); https://doi.org/10.1063/5.0104358

APL Quantum

CALL FOR APPLICANTS
Seeking Editor-in-Chief

AIP Publishing

Mode hybridization in DNA-inspired helical metamaterials with variable centro-asymmetry Ⓕ

Gunho Kim, Ⓘ Kaila M. Y. Coimbra, Ⓘ and Chiara Daraio[a) Ⓘ]

AFFILIATIONS

Division of Engineering and Applied Science, California Institute of Technology, Pasadena, California 91125, USA

[a)]Author to whom correspondence should be addressed: daraio@caltech.edu

ABSTRACT

We study helical acoustic metamaterials and demonstrate the ability to vary the materials' dispersion properties by controlling geometrical structure and mass distribution. By locally adding eccentric, higher density elements in the unit cells, we perturb the moment of inertia of the system and introduce centro-asymmetry. This allows controlling the degree of mode coupling and the width of subwavelength bandgaps in the dispersion relation, which are the product of enhanced local resonance hybridization. We characterize the distinct normal modes in our metamaterials using finite element simulations and analytically quantify the coupling between each mode. The evolution of acoustic bandgaps induced by the increasing level of centro-asymmetry is experimentally validated with 3D-printed structures.

Published under an exclusive license by AIP Publishing. https://doi.org/10.1063/5.0106740

Phononic crystals (PCs) and acoustic metamaterials (MMs) are rationally designed structured materials that can be engineered to control the propagation of acoustic and elastic waves. Traveling waves are reflected,[1–3] transmitted,[4] or guided,[5,6] depending on the geometry,[7,8] stiffness,[9,10] and structural composition.[11] Frequency bands of forbidden wave propagation (bandgaps) can be created by introducing Bragg scattering phenomena[12,13] or resonant structures.[14,15] Variations in the geometry or elastic modulus, achieved with electrical,[16] piezoelectric,[17] and mechanical stimuli[7,10] or via enhanced coupling between different vibrational modes,[18] have been used to manipulate the location and width of bandgaps.

PCs and MMs have been shown to present large controllability of their vibration and sound attenuation with structural elements that undergo deformations, like deflection or buckling.[7,19] Among these, chiral materials have been recently shown to support bandgap and mode tunability,[20,21] and they have also been studied for their unique mechanical properties,[22] like negative thermal expansion[23,24] and high impact absorption.[25] Chiral materials can be suggested as solutions for a number of industrial applications,[22] like airfoil stability[26] and catheters.[27] Recently, a new design of 3D chiral mechanical metamaterials has emerged and their dynamic properties have been characterized, showing distinctive wave modes, such as lifted degeneracy of two circularly polarized eigenmodes.[28,29] The role of centrosymmetry in chiral metamaterials and its effects on wave propagating properties have also been investigated in the context of tacticity.[30]

In this Letter, we study the dynamic characteristics of 3D-printed, chiral materials with a helicoidal shape (herein defined as helical metamaterials or HMMs). The HMMs are fabricated using a single acrylic polymer with added masses. We design their architecture to accommodate for centro-asymmetry, which allows for mode coupling and subwavelength bandgap formation. Leveraging these characteristics, we provide experimental evidence for the control of the HMMs' modal response and frequency bandgaps, making them a promising new class of materials for vibration isolation.

Inspired by the helicoidal configuration of Bouligand structures[31,32] and DNA[33] [Fig. 1(a)], we design and study a chiral structure consisting of horizontal beams, with radius $R = 2.5$ mm and length $L = 25$ mm, connected by thin, linear elastic pillars, with radius $r = 1.25$ mm and length $l = 6.6$ mm. These HMMs can be represented by a classical mass-spring system, where the horizontal beams function as discrete "masses" and the connecting pillars function as "springs." To ensure linear elastic interactions, we design pillars that are ten times lighter than the horizontal masses. Two connecting pillars, spaced 6.25 mm apart, are included between each beam for structural stability. To induce chirality, we rotate each mass-beam 45° with respect to its adjacent beam. We use the finite element method (FEM) to numerically analyze the normal modes of our metamaterials (COMSOL Multiphysics®). The normal modes of the HMMs excited by a plane wave traveling in the z-direction are shown in Fig. 1(b). The colors in Figs. 1(b) and 1(c) represent volumetric strain distribution, which shows that the deformation is mostly concentrated on the
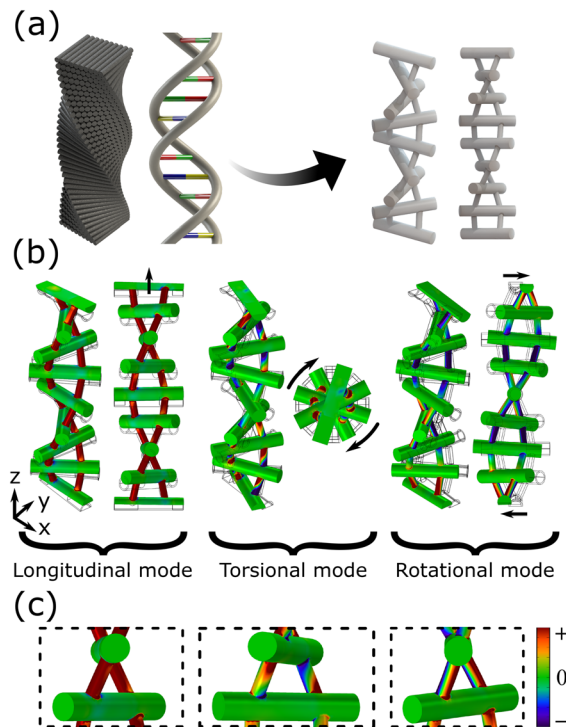
FIG. 1. Schematic of the samples' geometry and vibrational modes. (a) HMMs are inspired by Bouligand structures and the shape and aspect ratio of DNA molecules. (b) Normal modes of HMMs excited by a plane wave in the z-direction: longitudinal (left: isometric, right: side view), torsional (left: isometric, right: top view), and degenerate rotational mode (left: isometric, right: side view). Coordinate system indicates the coordinates of the isometric view. Black lines show the reference positions. (c) Truncated unit cells show different deformation behaviors of the connecting beams for each mode. The color shows volumetric strain distribution, where red indicates expansion and blue represents compression.
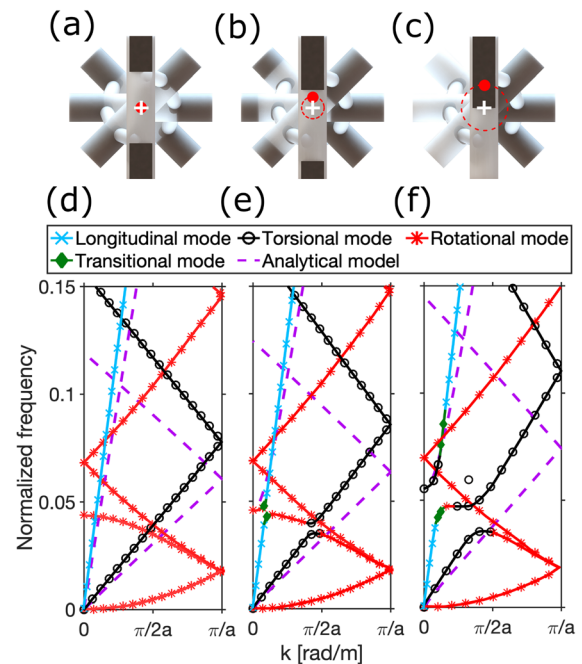

FIG. 2. (a)–(c) Top views of the HMMs model, which consists of two different materials (light gray: VeroWhite and black: stainless steel) with increasing centrosymmetry. The white cross shows the center axis of the HMMs and the red point shows the center of mass of the top beam. (d)–(f) Corresponding dispersion curves with normalized frequency as a function of wavenumber. The height of the unit cell a is 8 cm. Blue crosses, black circles, and red asterisks represent the longitudinal mode, the torsional mode, and the rotational mode, respectively. Orange points indicate the transitional modes between different types of normal modes, while the dashed purple lines represent the solution from the ladder-like analytical model.

connecting pillars. The longitudinal mode represents the motion parallel to the vertical axis, whereas the torsional mode generates a propagating twist. The strain distribution shows that the connecting pillars undergo tension and compression for the longitudinal mode, whereas they twist under the torsional mode. Because of the structure's chiral nature, expansion and compression of the longitudinal mode stimulate the torsional behavior of the HMMs, and vice versa. The rotational mode corresponds to a flexural mode, which bends the connecting pillars as they deform, while the chirality induces a propagating rotational wave around the central axis.

To analyze the effects of centrosymmetry on the acoustic characteristics of the HMMs, we adjust the center of mass of the horizontal beams, by inserting high-density stainless steel cylinders ($\rho = 7800 \, \text{kg/m}^3$) in precut holes on the beams' core. These high-density inserts are roughly seven times heavier than the base material used for the beams and connecting pillars (VeroWhite, $\rho = 1165 \, \text{kg/m}^3$, Stratasys™). When additional high-density inserts are arranged in one end of the beams, the beam's overall center of mass (red point) shifts further away from the central axis (white cross) of the HMMs [Figs. 2(a)–2(c)]. In all examples, we maintain the total mass and volume of the samples constant, by only re-positioning the steel inserts. We derive

the respective dispersion curves with normalized frequency and wavenumber [Figs. 2(d)–2(f)] using the FE model under the 1D Bloch periodic boundary condition. The frequency is normalized by the characteristic frequency of the longitudinal mode, which is the square root of the compressive stiffness divided by the mass of the horizontal cylinder. The wavenumber ranges from 0 to π/a, where a is the height of the unit cell ($a = 8 \, \text{cm}$). The different colored lines represent different wave modes, which are determined numerically. We used normalized volume-averaged displacements and curls to categorize the data points into longitudinal, torsional, and rotational modes. The blue line with $\times$ markers represents the dispersion characteristics of longitudinal waves. We identify the longitudinal mode by filtering through the modes with the normalized z-displacements greater than $\sqrt{2/3}$. Unsurprisingly, we note that longitudinal waves travel at the fastest speed, in comparison to other modes. The torsional mode (black circles) is the second fastest wave propagating through the structure, which is filtered by the higher volume-averaged curls ($>1/\sqrt{3}$) and the smaller volume-averaged displacements ($<1/\sqrt{2}$) in the z-direction. The slowest rotational mode (red asterisks) splits into two orthogonal modes, which arise from the chirality of the structure. The rotational modes are characterized by the larger lateral displacements, greater than $1/\sqrt{3}$, perpendicular to the central axis. For right-handed HMMs, a flexural wave rotating in the counterclockwise direction interacts with other modes and creates

partial bandgaps. A clockwise rotating flexural wave has minimal coupling with different modes and remains undisturbed even with strong centro-asymmetry. Other data points which do not fall into the above-mentioned categories are defined as transitional modes.

In the centrosymmetric structure, no apparent coupling between the existing modes is observed in the low frequency range [Fig. 2(d)]. As the structures become more centro-asymmetric, coupling between the different modes gets stronger and subwavelength longitudinal bandgaps emerge due to local resonance of the constituent elements.[34] We adopt a ladder-like metamaterials approach,[35] to develop an analytical model and quantify the coupling spring constant γ between the longitudinal mode and the rest of the modes. The derivation can be found in the supplementary material. The coupling constant gradually changes from 0 to 2.08 to 3.00 with increasing centro-asymmetry. We observe the widening of a longitudinal bandgap with enhanced coupling. The analytical model captures the slope of two branches that forms the longitudinal bandgap and shows the veering phenomena between the longitudinal mode and the torsional mode.[36] However, the model is based on two parallel mass-spring chains that are allowed to move in a single dimension only, which explains why it cannot fully grasp the complexity of the numerical solution.

To validate the numerical simulation results, we 3D-print periodic HMMs with varying levels of centro-asymmetry and characterize them experimentally [Fig. 3(b)]. We fabricate samples with six unit cells (= 48 cm) using a high-resolution PolyJet 3D printing technique (Stratasys Ltd., Connex 500). Due to the high aspect ratio of the samples, we use two minimally tensioned strings to hold the samples laterally from adjacent supports [Fig. 3(a)]. The base structures are built with VeroWhite acrylic photoresist, whose constituent properties are $E = 2.5$ GPa, $\nu = 0.33$,[37] and $\rho = 1165$ kg/m^3. We measure the stiffness of the VeroWhite acrylic polymer from dynamic characterization and the density using a regular scale. For the dynamic characterization, we measure the longitudinal wave speed of cylindrical samples with finite

length to derive the Young's modulus from the relation, $c_l = \sqrt{E/\rho}$. We use stainless steel mass inserts with $E = 200$ GPa, $\nu = 0.27$, and $\rho = 7800$ kg/m^3. Stainless steel rods (4 mm in diameter) are used as the weight inserts because of their high density, relative to VeroWhite. We use a piezoelectric transducer (Bruel & Kjaer, type 4810) to transmit the signal to the sample. Signals are generated by an arbitrary function generator (Keysight Technologies, 33522B), which is connected to a power amplifier (Bruel & Kjaer, type 2718). Hann-windowed three-cycle sinusoidal pulses are used to excite the lattices at a central frequency $f = 3$ kHz. We measure the transmitted pulse on the top surface of the sample using a laser Doppler vibrometer (Polytec, CLV-2534), which is sent to an oscilloscope (Tektronix, DPO 3014). The function generator and the oscilloscope are connected to a PC, which enable the integration of signal generation and data acquisition functionalities into a single MATLAB code.

Our FEM simulations predict that the size of the longitudinal bandgaps increases with higher levels of centro-asymmetry [Fig. 4(a)]. The deviation at the 0.625° comes from a transition of the longitudinal mode's coupling behavior. A more detailed description of the plot and the dispersion curves for all cases are included in the supplementary material. The transmission plots for the centrosymmetric case, the moderately centro-asymmetric case, and the fully centro-asymmetric case are shown in Fig. 4(b). The overlaying blue dots represent the longitudinal mode extracted from the dispersion curves, and the blue boxes highlight the longitudinal bandgaps identified through numerical simulations. The red boxes indicate where the transmission is less than −15 dB (∼18%) from the experimental results. The experimental tests show that the bandgaps are slightly shifted from the numerical simulations. The bandgap of the longitudinal mode widens as the HMMs become more centro-asymmetric, which coincides with the prediction. However, the subwavelength bandgaps at lower frequency range (<500 Hz) are not observed experimentally because the fabricated samples are not sufficiently tall to attenuate longer wavelength
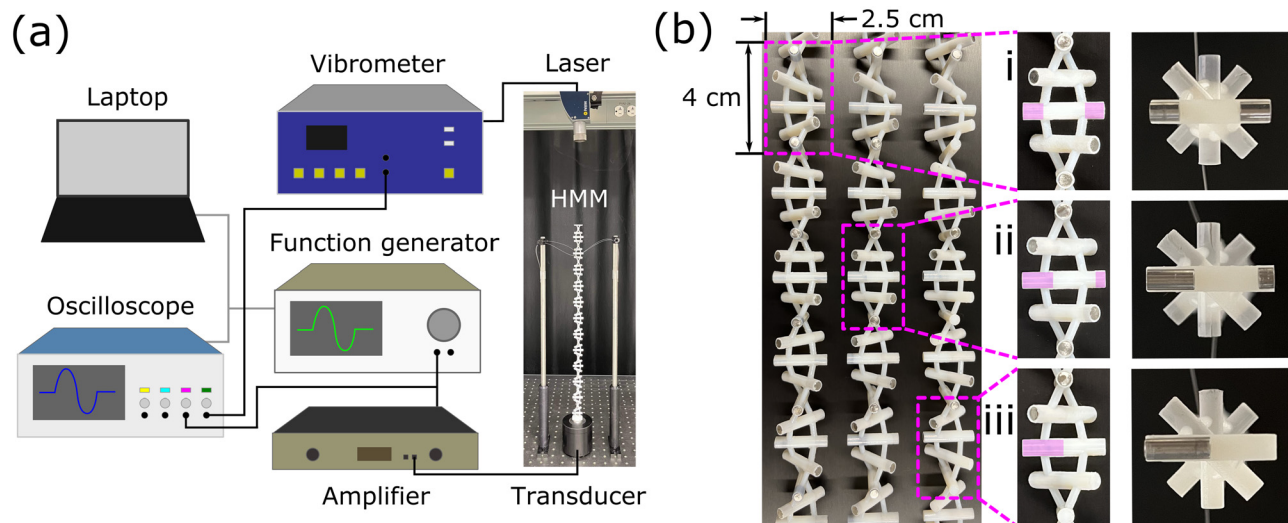

FIG. 3. (a) Schematic diagram and picture of the experimental setup for transmission measurements. (b) 3D-printed samples with added stainless steel inserts for varying centro-asymmetry: (i) 50–50 material distribution on both ends (centrosymmetric, 6.25:6.25 mm length ratio); (ii) 25–75 material distribution (moderately centro-asymmetric, 3.125:9.375 mm length ratio); and (iii) 0–100 material distribution (fully centro-asymmetric, 0:12.5 mm length ratio). Pink boxes indicate where the heavy inserts are positioned.
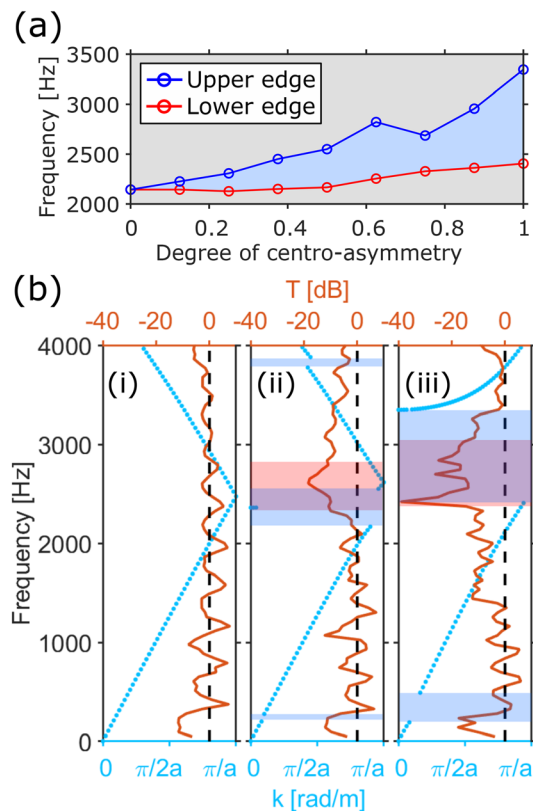
FIG. 4. (a) Numerically predicted evolution of the longitudinal bandgap (blue region) with increasing degree of centro-asymmetry. (b) Experimentally measured transmission curves (orange) are plotted with the longitudinal branch (blue dots) that is filtered from the dispersion curve of the (i) centrosymmetric, (ii) moderately centro-asymmetric, and (iii) fully centro-asymmetric HMMs. Plots are highlighted with blue shades indicating the longitudinal bandgaps predicted from the numerical simulation and red shades showing the transmission dips (< -15 dB).

inputs. The discrepancy between the numerical predictions and the test results originates from the presence of the torsional mode, which contributes to the longitudinal motion and can transfer the motion even within the longitudinal bandgap. Fabrication errors (either during machining or 3D-printing) and the need for support strings,[38] due to the long aspect ratio of the structures, may interfere with the measurements.

In summary, this work studies the mode hybridization induced by perturbed centrosymmetry in bioinspired, helical metamaterials. FEM and analytical studies show that the coupling intensity between independent modes grows with centro-asymmetry. We experimentally demonstrate the hybridization of propagating wave modes and the formation of partial bandgaps. In the future, the rich physics of chirality in acoustic metamaterials can be further studied for the realization of devices with acoustic polarization,[39] nonreciprocal wave propagation,[40] and mechanical logic switches.[41]

See the supplementary material for the derivation of the analytical model and the discussion on the hybridization phenomena.

AUTHOR DECLARATIONS
Conflict of Interest

The authors have no conflicts to disclose.

Author Contributions

Gunho Kim: Conceptualization (equal); Formal analysis (equal); Investigation (equal); Methodology (equal); Software (equal); Validation (equal); Visualization (equal); Writing – original draft (equal); Writing – review and editing (equal). **Kaila M. Y. Coimbra:** Conceptualization (lead); Investigation (supporting); Methodology (supporting); Software (supporting); Visualization (equal); Writing – original draft (equal); Writing – review and editing (equal). **Chiara Daraio:** Funding acquisition (equal); Project administration (equal); Supervision (equal); Writing – original draft (equal); Writing – review and editing (equal).

DATA AVAILABILITY

The data that support the findings of this study are available from the corresponding author upon reasonable request.

REFERENCES

[1]R. Martínez-Sala, J. Sancho, J. V. Sánchez, V. Gómez, J. Llinares, and F. Meseguer, "Sound attenuation by sculpture," Nature **378**, 241 (1995).
[2]Y. Pennec, J. O. Vasseur, B. Djafari-Rouhani, L. Dobrzyński, and P. A. Deymier, "Two-dimensional phononic crystals: Examples and applications," Surf. Sci. Rep. **65**, 229–291 (2010).
[3]M. I. Hussein, M. J. Leamy, and M. Ruzzene, "Dynamics of phononic materials and structures: Historical origins, recent progress, and future outlook," Appl. Mech. Rev. **66**, 040802 (2014).
[4]S. A. Cummer, J. Christensen, and A. Alù, "Controlling sound with acoustic metamaterials," Nat. Rev. Mater. **1**, 16001 (2016).
[5]V. Laude, "Principles and properties of phononic crystal waveguides," APL Mater. **9**, 080701 (2021).
[6]A. Mekis, J. C. Chen, I. Kurland, S. Fan, P. R. Villeneuve, and J. D. Joannopoulos, "High transmission through sharp bends in photonic crystal waveguides," Phys. Rev. Lett. **77**, 3787–3790 (1996).
[7]K. Bertoldi and M. C. Boyce, "Mechanically triggered transformations of phononic band gaps in periodic elastomeric structures," Phys. Rev. B **77**, 052105 (2008).
[8]P. Wang, F. Casadei, S. Shan, J. C. Weaver, and K. Bertoldi, "Harnessing buckling to design tunable locally resonant acoustic metamaterials," Phys. Rev. Lett. **113**, 014301 (2014).
[9]C. Daraio, V. F. Nesterenko, E. B. Herbold, and S. Jin, "Tunability of solitary wave properties in one-dimensional strongly nonlinear phononic crystals," Phys. Rev. E **73**, 026610 (2006).
[10]F. Li, C. Chong, J. Yang, P. G. Kevrekidis, and C. Daraio, "Wave transmission in time- and space-variant helicoidal phononic crystals," Phys. Rev. E **90**, 053201 (2014).
[11]E. Dong, Z. Song, Y. Zhang, S. G. Mosanenzadeh, Q. He, X. Zhao, and N. X. Fang, "Bioinspired metagel with broadband tunable impedance matching," Sci. Adv. **6**, eabb3641 (2020).
[12]M. M. Sigalas and E. N. Economou, "Elastic and acoustic wave band structure," J. Sound Vib. **158**, 377–382 (1992).

[13]M. Sigalas and E. N. Economou, "Band structure of elastic waves in two dimensional systems," Solid State Commun. **86**, 141–143 (1993).

[14]Z. Liu, X. Zhang, Y. Mao, Y. Y. Zhu, Z. Yang, C. T. Chan, and P. Sheng, "Locally resonant sonic materials," Science **289**, 1734–1736 (2000).

[15]N. Fang, D. Xi, J. Xu, M. Ambati, W. Srituravanich, C. Sun, and X. Zhang, "Ultrasonic metamaterials with negative modulus," Nat. Mater. **5**, 452–456 (2006).

[16]S. Xiao, G. Ma, Y. Li, Z. Yang, and P. Sheng, "Active control of membrane-type acoustic metamaterial by electric field," Appl. Phys. Lett. **106**, 091904 (2015).

[17]L. Airoldi and M. Ruzzene, "Design of tunable acoustic metamaterials through periodic arrays of resonant shunted piezos," New J. Phys. **13**, 113010–113021 (2011).

[18]D. Beli, J. R. F. Arruda, and M. Ruzzene, "Wave propagation in elastic metamaterial beams and plates with interconnected resonators," Int. J. Solids Struct. **139–140**, 105–120 (2018).

[19]M. Miniaci, M. Mazzotti, A. Amendola, and F. Fraternali, "Effect of prestress on phononic band gaps induced by inertial amplification," Int. J. Solids Struct. **216**, 156–166 (2021).

[20]A. Spadoni and M. Ruzzene, "Structural and acoustic behavior of chiral truss-core beams," J. Vib. Acoust. **128**, 616–626 (2006).

[21]A. Spadoni, M. Ruzzene, S. Gonella, and F. Scarpa, "Phononic properties of hexagonal chiral lattices," Wave Motion **46**, 435–450 (2009).

[22]W. Wu, W. Hu, G. Qian, H. Liao, X. Xu, and F. Berto, "Mechanical design and multifunctional applications of chiral mechanical metamaterials: A review," Mater. Des. **180**, 107950 (2019).

[23]R. Lakes, "Cellular solid structures with unbounded thermal expansion," J. Mater. Sci. Lett. **15**, 475–477 (1996).

[24]C. S. Ha, E. Hestekin, J. Li, M. E. Plesha, and R. S. Lakes, "Controllable thermal expansion of large magnitude in chiral negative Poisson's ratio lattices," Phys. Status Solidi B **252**, 1431–1434 (2015).

[25]A. Spadoni, M. Ruzzene, and F. Scarpa, "Global and local linear buckling behavior of a chiral cellular structure," Phys. Status Solidi B **242**, 695–709 (2005).

[26]D. Bornengo, F. Scarpa, and C. Remillat, "Evaluation of hexagonal chiral structure for morphing airfoil concept," Proc. Inst. Mech. Eng., Part G **219**, 185–192 (2005).

[27]W. Wu, Y. Tao, Y. Xia, J. Chen, H. Lei, L. Sun, and D. Fang, "Mechanical properties of hierarchical anti-tetrachiral metastructures," Extreme Mech. Lett. **16**, 18–32 (2017).

[28]T. Frenzel, M. Kadic, and M. Wegener, "Three-dimensional mechanical metamaterials with a twist," Science **358**, 1072–1074 (2017).

[29]T. Frenzel, J. Köpfler, E. Jung, M. Kadic, and M. Wegener, "Ultrasound experiments on acoustical activity in chiral mechanical metamaterials," Nat. Commun. **10**, 3384 (2019).

[30]A. Bergamini, M. Miniaci, T. Delpero, D. Tallarico, B. Van Damme, G. Hannema, I. Leibacher, and A. Zemp, "Tacticity in chiral phononic crystals," Nat. Commun. **10**, 4525 (2019).

[31]I. Kellersztein, S. R. Cohen, B. Bar-On, and H. D. Wagner, "The exoskeleton of scorpions' pincers: Structure and micro-mechanical properties," Acta Biomater. **94**, 565–573 (2019).

[32]I. Greenfeld, I. Kellersztein, and H. D. Wagner, "Nested helicoids in biological microstructures," Nat. Commun. **11**, 224 (2020).

[33]K. W. Olsen and J. Bohr, "Transcription and the aspect ratio of DNA," New J. Phys. **15**, 093008 (2013).

[34]M. I. H. A. Srikantha Phani, *Dynamics of Lattice Materials* (Wiley, 2017).

[35]S. Hajarolasvadi and A. E. Elbanna, "Dispersion properties and dynamics of ladder-like meta-chains," Extreme Mech. Lett. **43**, 101133 (2021).

[36]B. R. Mace and E. Manconi, "Wave motion and dispersion phenomena: Veering, locking and strong coupling effects," J. Acoust. Soc. Am. **131**, 1015–1028 (2012).

[37]S. Cui, B. Gong, Q. Ding, Y. Sun, F. Ren, X. Liu, Q. Yan, H. Yang, X. Wang, and B. Song, "Mechanical metamaterials foams with tunable negative Poisson's ratio for enhanced energy absorption and damage resistance," Materials **11**, 1869 (2018).

[38]K. Pajunen, P. Celli, and C. Daraio, "Prestrain-induced bandgap tuning in 3D-printed tensegrity-inspired lattice structures," Extreme Mech. Lett. **44**, 101236 (2021).

[39]A. S. Pine, "Direct observation of acoustical activity in α quartz," Phys. Rev. B **2**, 2049–2054 (1970).

[40]Y. Wang, B. Yousefzadeh, H. Chen, H. Nassar, G. Huang, and C. Daraio, "Observation of nonreciprocal wave propagation in a dynamic phononic lattice," Phys. Rev. Lett. **121**, 194301 (2018).

[41]B. Zheng and J. Xu, "Mechanical logic switches based on DNA-inspired acoustic metamaterials with ultrabroad low-frequency band gaps," J. Phys. D **50**, 465601 (2017).